Springer

KSME

Journal of Mechanical Science and Technology 31 (1) (2017) 215~224
www.springerlink.com/content/1738-494x(Print)/1976-3824(Online)
DOI 10.1007/s12206-016-1224-0

Numerical simulation of the sheet/cloud cavitation around a two-dimensional hydrofoil using a modified URANS approach †

Zhong Li[1,*], Dawei Zheng[1], Feng Hong[2], and Dan Ni[1]

[1]*School of Energy and Power Engineering, Jiangsu University, Zhenjiang, 212013, China*
[2]*Research Center of Fluid Machinery Engineering and Technology, Jiangsu University, Zhenjiang, 212013, China*

(Manuscript Received March 15, 2016; Revised July 15, 2016; Accepted August 9, 2016)

Abstract

Cavitating flow over a two-dimensional Clark-Y hydrofoil is numerically investigated via a Modified density correction method (MDCM) for turbulence closure to improve the capability of two-phase flow simulation for the *k-ε* RNG turbulence model. A transport equation model for the local volume fraction of vapor is solved, and a modified version of the Kunz model is used for the condensation and evaporation processes. Simulations have been conducted for various cavitation numbers ranging from non-cavitating to cloud cavitation. We compared the time-averaged lift and drag coefficients, cavitation dynamics, and time-averaged velocity profiles with the available experimental data for the MDCM and Density correction method (DCM). The comparisons between numerical and experimental results show that the MDCM and DCM are capable of capturing the special trends of the lift coefficient at the inception cavitation stage and the drag coefficient at the cloud cavitation stage. The MDCM is more robust and physical than the DCM in predicting the wake flow downstream from the trailing edge. The predicted attached cavities of both models almost show the same trend near the leading edge of the hydrofoil. However, the MDCM predicts more shedding cavity than the DCM in the wake region.

Keywords: Cavitating flow; DCM; Hydrofoil; Numerical simulation

1. Introduction

Cavitation is the phenomenon that involves the formation and activity of cavities inside a liquid medium. Cavitation usually occurs when the liquid pressure becomes less than the vapor pressure. Cavitation can occur in a wide variety of fluid machinery, such as pumps, marine propellers, and hydrofoils. Many investigators have examined numerous aspects of cavitation over the past decades [1-3]. However, the physical mechanisms of cavitation are not well understood because of the complex, unsteady flow structures associated with turbulence and cavitation dynamics. Significant computational issues with regard to the stability, efficiency, and robustness of the numerical algorithm for turbulent unsteady cavitating flows have been investigated [4].

In the past two decades, considerable efforts have been exerted in the numerical methods for unsteady cavitating flows. A well-known technique is to apply the assumption of homogeneous medium in equilibrium, as proposed by Kubota, in which the slip between vapor and liquid at the interface is neglected and the two-phase mixture is treated as a single fluid [5]. The mixture density definition and resolution, which induce various modeling approaches, are also considered. One well-known definition is based on the barotropic state law initially developed by Delannoy and Kueny [6]. In 2003, Coutier-Delgosha et al. [7] used this method to simulate cloud cavity shedding in a Venturi-type duct. The other method is known as the transport equation-based cavitation model, in which the advection equation for liquid or vapor volume fraction is solved. Steady and unsteady flow computations based on this model have been reported by many researchers, such as Kubota et al. [8], Singhal et al. [9], Merkle et al. [10], Kunz et al. [11], and Senocak et al. [12].

The implementation of a suitable turbulence model is important for the accurate prediction of cavitation because cavitating flows occur at high Reynolds numbers and unsteady conditions. Rebound et al. [13] and Coutier-Delgosha et al. [14] developed a modified *k-ε* turbulence model, in which turbulence viscosity is corrected by multiplying with the function $f(\rho_m)$, to solve the problem of large density jump in the cavity closure region. Rebound et al. [13] and Coutier-Delgosha et al. [14] successfully applied this model in the cavitating flow simulations of a Venturi-type duct. Notably, the modified *k-ε* model could better predict the cloud cavity shedding downstream and the generation of unsteady reentrant

*Corresponding author. Tel.: +86 511 88783105, Fax.: +86 511 88783105
E-mail address: lizhong@ujs.edu.cn
† Recommended by Associate Editor Shin Hyung Rhee

jet flow. However, the simulation results under low cavitation numbers were unable to determine the shedding frequency and cavity length accurately compared with the experimental data. Recently, hybrid modeling approaches have emerged to improve the traditional Reynolds-averaged Navier-Stokes (RANS) models, such as detached eddy simulation [15], Filter-based model (FBM) [16], partially averaged Navier-Stokes model [17], and many versions of the RANS/LES hybrid models. Indeed, these hybrid models have significantly improved the predictions of single-phase flows. Moreover, some of these hybrid models have been applied to successfully simulate cavitating flows around hydrofoils and obtain encouraging results compared with the traditional RANS models.

Inspired by the previous reporters, the present study focused on improving the predictive capability of the *k-ε* RNG turbulence model via a Modified density correction method (MDCM) for turbulence closure. A numerical simulation of the sheet/cloud unsteady cavitating flows around a two-dimensional (2D) Clark-Y hydrofoil is conducted to assess the numerical method. Comparisons between numerical results and available experimental data in the literature are performed to evaluate the method and help further understand the cavitation dynamics. The present paper is organized as follows: Sec. 2 presents the mathematical and numerical methods employed in this study. Sec. 3 presents the numerical setup and description. Sec. 4 provides the detailed results and discussions. Sec. 5 gives the concluding remarks.

2. Numerical model

2.1 Conservation of mass and momentum

The conservation forms of the URANS equations for Newtonian fluid without body forces and heat transfers are presented along with the mass transport equation in the Cartesian coordinates [18], as follows:

$$\frac{\partial \rho_m}{\partial t}+\frac{\partial(\rho_m u_j)}{\partial x_j}=0\,, \tag{1}$$

$$\frac{\partial}{\partial t}\left(\rho_m u_i\right)+\frac{\partial}{\partial x_j}\left(\rho_m u_i u_j\right)=-\frac{\partial p}{\partial x_i} +\frac{\partial}{\partial x_j}\left[(\mu_m+\mu_t)\left(\frac{\partial u_i}{\partial x_j}+\frac{\partial u_j}{\partial x_i}-\frac{2}{3}\frac{\partial u_k}{\partial x_k}\delta_{ij}\right)\right], \tag{2}$$

$$\frac{\partial(\rho_v\alpha_v)}{\partial t}+\frac{\partial}{\partial x_j}(\rho_v u_j\alpha_v)=S_e-S_c\,, \tag{3}$$

$$\rho_m=\alpha_v\rho_v+(1-\alpha_v)\rho_l\,, \tag{4}$$

$$\mu_m=\alpha_v\mu_v+(1-\alpha_v)\mu_l\,, \tag{5}$$

where ρ_m denotes the mass density of the mixture; u is the velocity of the mixture; p is the pressure; μ_m and μ_t are the molecular and turbulence viscosities obtained from the turbulence model, respectively; ρ_l and ρ_v represent the density of liquid and vapor, respectively; α_v is the volume fraction of vapor, μ_l and μ_v are the liquid and vapor dynamic viscosities, respectively; and S_e and S_c describe the source terms for the evaporation and condensation processes, respectively.

2.2 Cavitation model

In the present work, a modified version of the Kunz model is adopted for mass transfer modeling. The mass transfer terms are based on the mass conservation of liquid and vapor. Evaporation, S_e, is modeled to be proportional to the amount of liquid present and the difference between liquid pressure and vapor pressure, whereas condensation, S_c, is based on the third-order polynomial function of the vapor volume fraction [11]. This model is similar to that used by Merkle et al. [10] for the evaporation and condensation processes. The advection equation for the vapor volume fraction is solved in ANSYS Fluent, and the cavitation process is governed by the local volume fraction transport equation when the Kunz model is applied, as follows:

$$\frac{\partial\left(\rho_v\alpha_v\right)}{\partial t}+\frac{\partial}{\partial x_j}\left(\rho_v u_j\alpha_v\right)=-\frac{C_{prod}\rho_v^2(1-\alpha_v)^2\alpha_v}{p_l t_\infty} -\frac{C_{dest}\rho_v^2(1-\alpha_v)\min(p-p_v,0)}{0.5\rho_l^2U_\infty^2 t_\infty}\,, \tag{6}$$

where C_{dest} and C_{prod} are empirical constants ($C_{dest} = 2.0 \times 10^4$ and $C_{prod} = 1.0 \times 10^3$, as suggested in Ref. [19]). The mass transfer rates are nondimensionalized with respect to the mean flow timescale, $t_\infty = L_{ch}/U_\infty$, where L_{ch} is the characteristic length and U_∞ is the free stream velocity.

2.3 Modified density correction method

The unsteady cyclic behavior in the sheet/cloud cavitation flow around a hydrofoil is strongly dependent on the turbulence model. A standard two-equation turbulence model is unable to resolve this unsteadiness. The reentrant jet flow is stopped before breaking the cavity interface and the oscillating characteristics of the cavity never occur if the standard *k-ε* turbulence model is applied. Therefore, such two-equation turbulence models tend to overestimate the turbulent eddy viscosity in the region of transition between vapor and liquid phases and dampen the unsteadiness of the cavitating regime [13, 14]. Rebound et al. [13] proposed a simple modification of the *k-ε* turbulence model by artificially reducing the turbulent viscosity to consider the proposed two-phase flow effects on the turbulent structures. The turbulent viscosity is multiplied with the function $f(\rho_m)$ to reduce the turbulent viscosity in the region of cavity closure. $f(\rho_m)$ is defined as:

$$f(\rho_m)=\frac{\rho_v+(1-\alpha_v)^n(\rho_l-\rho_v)}{\rho_v+(1-\alpha_v)(\rho_l-\rho_v)}\,,\ \text{with}\ n\geq 1. \tag{7}$$

The density function $f(\rho_m)$ will be equal to 1 in the regions

with pure water and vapor, but changes rapidly in the two-phase mixture flows. Thus, the modified kinetic eddy viscosity $\mu_{T\text{-}DCM}$ in the k-ε RNG turbulence model reads:

$$\mu_{T-DCM} = \frac{C_\mu \rho_m k^2}{\varepsilon} f(\rho_m), \text{ with } C_\mu = 0.09. \tag{8}$$

Common choices for the exponent in Eq. (7), which are considered to be sufficient for most applications, are $n = 3$ or $n = 10$. Seo et al. [20] and Ducoin et al. [21] concluded that $n = 3$ is a better choice for cavitating flows around a hydrofoil; thus, $n = 3$ has been used in all numerical simulations reported in this study.

In addition to the density correction approach, Johansen et al. [16, 22] proposed the FBM to improve the predictive capability of the standard k-ε two-equation turbulence model. Given the fact that the true resolution is dictated not only by the mesh size, Δ_{grid}, but also by the magnitude of the eddy viscosity, v_{eff}, in the RANS computations, the turbulent eddy viscosity can be modified using the following equations:

$$f_{FBM} = \min\left\{1, C_3 \frac{\lambda \cdot \varepsilon}{k^{3/2}}\right\}, \tag{9}$$

$$\mu_{T-FBM} = \frac{C_\mu \rho_m k^2}{\varepsilon} f_{FBM}, \tag{10}$$

where $k^{3/2}/\varepsilon$ represents the local turbulence length scale, λ denotes the filter size, $C_\mu = 0.09$ and $C_3 = 1.0$.

In the near-wall regions of the hydrofoil, the size of the local mesh is larger than the turbulence length scale, that is, $\lambda >> k^{3/2}/\varepsilon$. Then, Eq. (10) yields $\mu_{T\text{-}FBM} = C_\mu \rho_m k^2/\varepsilon$, and the original k-ε two-equation turbulence model is recovered. By contrast, in the regime far from the surface, the turbulence length scale is greater than the local mesh size, that is, $k^{3/2}/\varepsilon >> \lambda$. Then, the turbulent viscosity $\mu_{T\text{-}FBM} = C_\mu \rho_m \lambda k^{1/2}$. Therefore, the filter-based approach is originally proposed to ensure that the turbulent viscosity is always lower than the RANS value in stagnation flows. Particularly, the FBM can be applied to reduce the turbulent eddy viscosity in the cavitating wake flows, where the Density correction method (DCM) is not sufficiently robust to limit the turbulent viscosity because less density jump exists in the shedding cloud cavity. Therefore, the filter-based method can be adopted to improve the prediction of cavitation dynamics in wake flow by enabling the shedding cavity to move and collapse downstream.

DCM and FBM are developed to limit the kinematic turbulent viscosity. However, these methods work in different computational regions. MDCM that overcomes the disadvantage of DCM, which only works in the near-wall cavitation regime, is employed to limit the turbulent eddy viscosity in the cavitation regime near the hydrofoil surface and cavitating wake flows. The modified turbulent viscosity based on MDCM reads:

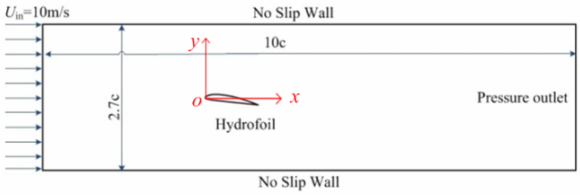

Fig. 1. Computational domain and boundary conditions.

$$\mu_{T-MDCM} = \frac{C_\mu \rho_m k^2}{\varepsilon} f_{hybrid}, \tag{11}$$

$$f_{hybrid} = \min\left\{f(\rho_m), C_3 \frac{\lambda \cdot \varepsilon}{k^{3/2}}\right\}, \tag{12}$$

where $f(\rho_m)$ is estimated from Eq. (7) and all the constants remain the same as that of FBM and DCM. The hybrid function f_{hybrid} is used to blend the two models, which will help limit the overprediction of the turbulent eddy viscosity in the cavitating regions on the wall of hydrofoil and in the wake flow downstream.

3. Numerical setup and description

3.1 Numerical setup

The numerical results of this study correspond to a hydrofoil at a fixed attack angle of $\alpha = 8°$ and are subject to a nominal free stream velocity of $U_\infty = 10$ m/s. With chord length $c = 70$ mm, we obtain $Re = 6.14 \times 10^5$. The density and dynamic viscosity of the liquid are $\rho_l = 999.19$ kg/m^3 and $\mu_l = 1.139 \times 10^{-3}$ Pa·s, respectively, which correspond to fresh water at 25 °C. The vapor density is $\rho_v = 0.02308$ kg/m^3 and the vapor viscosity is $\mu_v = 9.8626 \times 10^{-6}$ Pa·s. The saturation pressure of water at 25 °C is $p_{sat} = 3169$ Pa.

The computational domain and boundary conditions are consistent with the experimental setup described in Ref. [18] and are shown in Fig. 1. The velocity inlet condition is applied at the upstream inflow, and the pressure outlet condition is applied at the outlet boundary. The top and bottom walls are regarded as no-slip wall. The turbulent intensity at the inlet boundary is set as $I = 2$ % according to the experimental measurements. Two important nondimensional numbers, that is, the Reynolds number and the cavitation number, are defined using the properties of the incoming flow in the following manner:

$$\mathrm{Re} = \frac{\rho_l U_\infty c}{\mu_l}, \tag{13}$$

$$\sigma = \frac{p_{out} - p_{sat}}{0.5 \rho_l U_\infty^2}, \tag{14}$$

where p_{out} is the pressure at the outlet that determines the cavitation numbers, p_{sat} is the saturation pressure of vapor, and U_∞ is the free stream velocity that is equal to 10 m/s.

3.2 Numerical strategy

The ANSYS Fluent code employs the node-centered finite volume method. The numerical strategy applies the pressure-based coupled RANS solver, accelerated by the algebraic multigrid method, to solve the governing equations with a fully implicit discretization in time. The PISO-type pressure-velocity coupling correction method for the arbitrary Mach number is employed; this algorithm uses iterative calculations to solve the pressure and velocity equations.

A second-order implicit transient formulation is used for the time-dependent computation to acquire a relatively accurate resolution of the cavitation collapse. Second-order discretization schemes are used for pressure, density, momentum, turbulence kinetic energy, and dissipation rate. The QUICK scheme is used for the vapor phase transport equation. The Green-Gauss node-based method is used to compute the gradients of the variables appearing in the governing equations. Under-relaxation factors (URFs) are vital for cavitation simulations because the order-of-magnitude difference of the densities of the two phases and the large pressure gradient cause numerical instability. Low to moderate values (between 0.25 and 0.5) are assigned for pressure, momentum, and volume fraction URFs. For density, vaporization mass, turbulence kinetic energy, turbulent dissipation rate, and turbulent eddy viscosity, average to high URFs work better (between 0.5 and 1.0).

The enhanced wall treatment considering the pressure gradient effects is adopted for the ε equation of the k-ε RNG turbulence model to achieve the goal of having a near-wall modeling approach that will process the accuracy of the standard two-layer approach for fine near-wall meshes and will not significantly reduce the accuracy of wall function meshes. The enhanced wall treatment is a near-wall modeling method that combines a two-layer model with the so-called wall functions. If the near-wall mesh is sufficiently fine, typically with the first near-wall node placed at $y^+ \approx 1$, then the viscous sublayer can be resolved and the enhanced wall treatment will be identical to the traditional two-layer zone model [23].

The steady results for non-cavitating were used as initial solutions for the unsteady cavitating flow simulations. The unsteady solution converges when the tracked monitor shows periodic convergence. The Courant-Friedrichs-Lewy condition is used to determine the time step in which the first element near the hydrofoil was selected, as follows:

$$\Delta t = \frac{C_{\max}}{\frac{U_\infty}{\Delta x}} \approx \frac{1}{\frac{10}{2.5e^{-6}}} = 2.5e^{-7}\text{s} . \quad (15)$$

Simulations for time steps of $\Delta t = 1 \times 10^{-8}$, 1×10^{-7} and 2×10^{-6} are performed. All of these time steps converge to the same level. Thus, the value of $\Delta t = 2 \times 10^{-6}$ s is selected for all unsteady calculations to reduce the calculation resources and computational time.

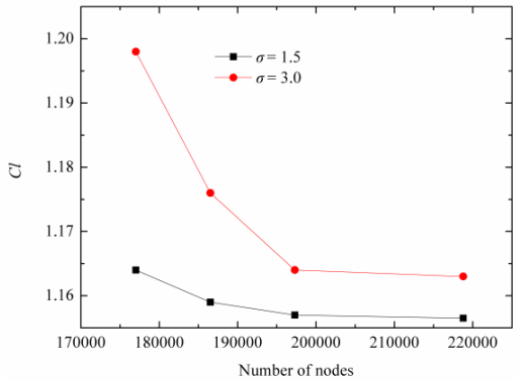

Fig. 2. Comparisons of the predicted lift coefficients between different grids under non-cavitating and cavitating conditions.

4. Results and discussion

4.1 Mesh independence study

As the Clark-Y hydrofoil is not geometrically complex, the structured quadrilateral meshes are adopted in our work. The blocking strategy, that is, a C-block is wrapped around the hydrofoil embedded in an H-block, is shown in Fig. 3(a). The mesh sensitivity and mesh convergence are investigated on four grids with different densities but with similar multi-block topology, resulting in a total of 16 blocks. The lift coefficient is selected as the parameter of interest for the mesh convergence study. Four sets of block-structured quadrilateral meshes with different qualities are used for this analysis. The results based on the simulations with two different cavitation numbers were obtained.

Fig. 2 shows the comparison of the predicted lift coefficients between different grids for the non-cavitating (σ = 3.0) and cavitating (σ = 1.5) conditions. The figure also shows that a grid of 197296 is sufficient, as no further convergence is observed when the grid is increased to 218776 under non-cavitating and cavitating conditions. The difference of lift coefficient between two largest meshes is less than 1 % for both simulations. Therefore, grid 3 was used for all subsequent calculations. Fig. 3 illustrates the entire block and the detailed meshes near the leading and trailing edges of the hydrofoil. A growth factor of 1.15 is used to ensure that many cells are placed inside the boundary layer. The element quality for all meshes is greater than 0.8, which is well above the value of 0.3 required by the solver as a rule of thumb. The y^+ values in the order of unity using grid 3 is shown in Fig. 4. The calculated y^+ value after simulation is 1.3 close to the leading edge and less than 0.8 for the remainder of the hydrofoil. The enhanced wall treatment method requires a mesh of $y^+ \approx 1$ near the wall of the computational domain [23]; therefore, the near-wall cells satisfy the requirement of the turbulence model. The distribution of the pressure coefficient, C_p, at the wall after calculation is shown in Fig. 5, and the results obtained are consistent with the simulation results and the available experimental data obtained from Ref. [24].

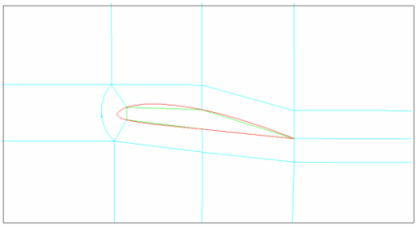

(a) Blocking strategy for the 2D hydrofoil after being zoomed

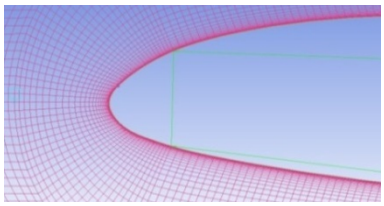

(b) Mesh near the leading edge

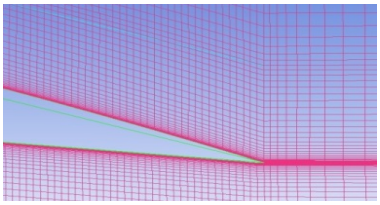

(c) Mesh near the trailing edge

Fig. 3. Entire block for the computational domain and detailed meshes near the two edges.

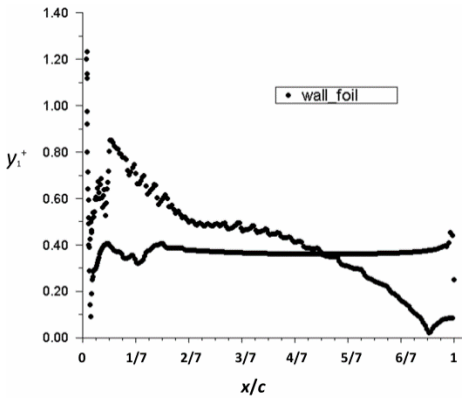

Fig. 4. Wall y+ distribution around the hydrofoil.

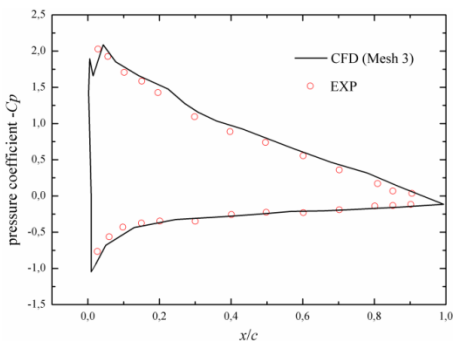

Fig. 5. Surface pressure coefficient of the hydrofoil, in which the experimental data are obtained from Ref. [24].

Table 1. Lift and drag coefficients based on different filter sizes.

	$0.8\Delta_{max}$	$1.5\Delta_{max}$	$2.5\Delta_{max}$	$3.5\Delta_{max}$	k-ε RNG	EXP [2]
C_l	0.739	0.736	0.718	0.702	0.692	0.76
C_d	0.116	0.116	0.114	0.112	0.108	0.119

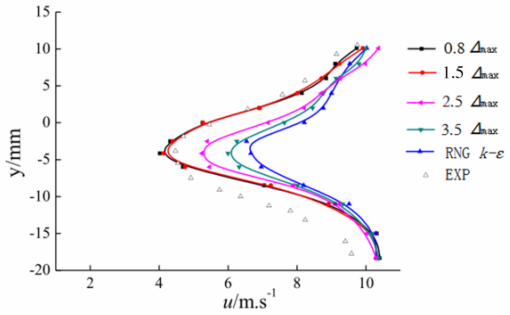

Fig. 6. Time-averaged x-velocity at x/c = 1.0 based on filter sizes.

4.2 Filter size independence study

The MDCM combines the strengths of the DCM and FBM; however, the capability of the MDCM to accurately predict the cavitation dynamics is based on a suitable filter size λ. Eq. (9) shows that the FBM is similar to the original RANS method when a large value is selected for the filter size λ. Thus, selecting a suitable filter size for the numerical simulation of sheet/cloud cavitation around the hydrofoil is important. A filter size independence study was performed based on the largest local O-shape grid near the surface of the hydrofoil, which is set as $\Delta_{max} = 0.004c$. Four different filter sizes λ, that is, $0.8\Delta_{max}$, $1.5\Delta_{max}$, $2.5\Delta_{max}$ and $3.5\Delta_{max}$, were selected to calculate the cloud cavitating flows.

Fig. 6 shows the time-averaged x-velocity component profiles along the wall-normal direction at x/c = 1.0 based on different filter sizes for cloud cavitation ($\sigma = 0.8$). As observed, the time-averaged x-velocity becomes closer to the experimental results when the filter size decreases and the predicted results of $\lambda = 0.8\Delta_{max}$ and $\lambda = 1.5\Delta_{max}$ are consistent with the experimental results. Table 1 shows the comparisons of the drag and lift coefficients between the simulation results obtained from different filter sizes and the available experimental data at a cavitation number of σ = 0.8. Notably, no further convergence is reached when the filter size is decreased to $1.5\Delta_{max}$ compared with the results of $0.8\Delta_{max}$. The drag and lift coefficients predicted using $1.5\Delta_{max}$ are consistent with the experimental results. Thus, selecting the filter size $\lambda = 1.5\Delta_{max}$ is appropriate.

4.3 Characteristics of the drag and lift coefficients

The comparisons of the time-averaged drag and lift coefficients using the DCM and MDCM in the entire range of operating conditions from non-cavitating to cloud cavitation are shown in Fig. 7. The available experimental data from Ref. [25] are also provided. These time-averaged coefficients are

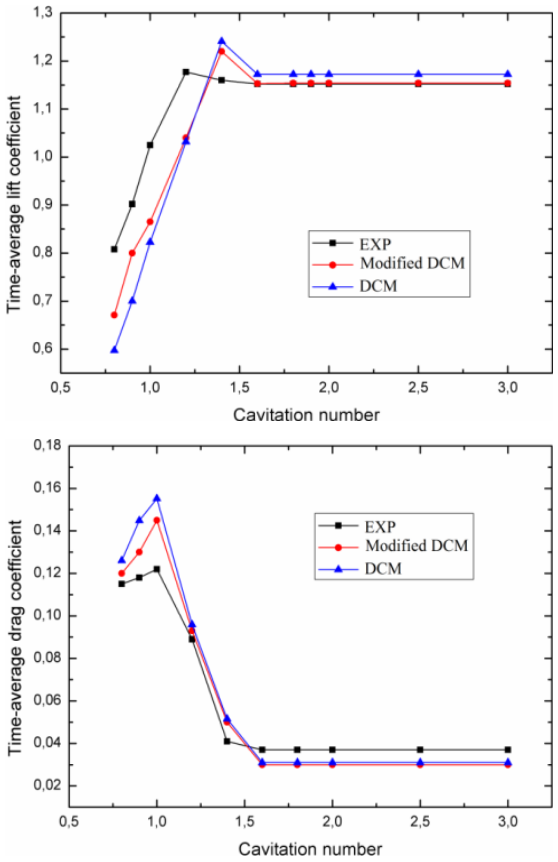

Fig. 7. Time-averaged coefficients between DCM and MDCM. Experimental data from Ref. [25] are provided where available. Top: Comparisons of the time-averaged lift coefficients; bottom: Comparisons of the time-averaged drag coefficients.

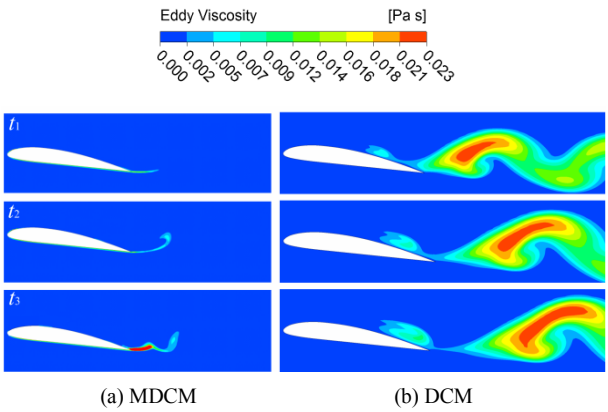

(a) MDCM (b) DCM

Fig. 8. Predicted turbulent eddy viscosity by different turbulence models for cloud cavitation at three instances ($\sigma = 0.8$).

obtained from the entire instantaneous results of each iteration for different cavitation numbers, which make the coefficients more accurate. When the flow is non-cavitating, for cavitation numbers between 1.6 and 3.0, the lift and drag coefficients remain unchanged for the predicted values and the experimental results. In this range, the predicted lift coefficients from the MDCM are consistent with the experimental results; however,

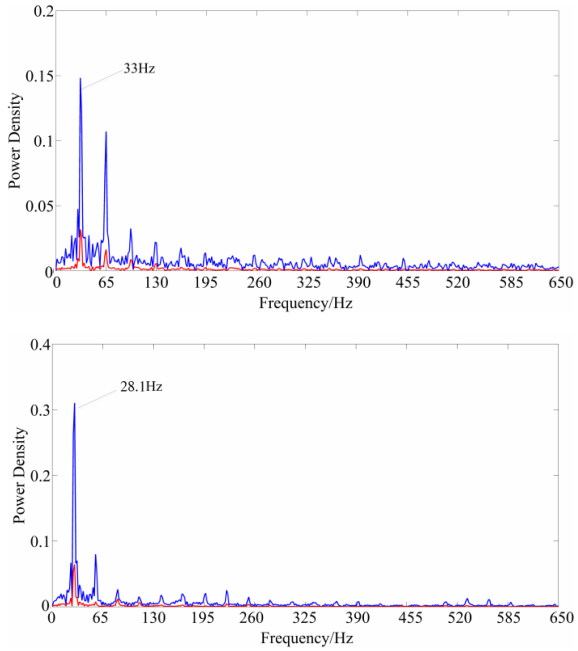

Fig. 9. Shedding frequency based on FFT analysis of the time history of the lift (red line) and drag (blue line) coefficients for cloud cavitation. Top: Frequency of the DCM; bottom: Frequency of the MDCM.

the results from DCM are higher than that of the experimental results. By contrast, in non-cavitating flows, the predicted drag coefficients obtained using the DCM and MDCM are close to each other and are lower than the experimental results. When the flow is cavitating, the corresponding cavitation number is lower than 1.6 and the MDCM predicts more accurate lift and drag coefficients than the DCM. This finding can be explained by the small difference of the turbulent eddy viscosity applied in these models, that is, the MDCM helps limit the overassessment of the turbulent viscosity not only in the cavitating regions near the leading edge of the hydrofoil but also in the wake flow downstream, as shown in Fig. 8. In the cavitation inception stage, cavitation occurs in the form of traveling bubbles, which cause a slight increase in the lift and drag coefficients. As observed, the turbulence models are capable of predicting such increasing trend combined with the Kunzcavitation model. Particularly, in cloud cavitation, the vortex shedding and related unsteady movement strongly affect the flow structure around the hydrofoil, leading to the maximum drag coefficient. Notably, this maximum value of the drag coefficient is derived by both turbulence models; however, the MDCM predicts a closer value than that of DCM compared with the experimental data.

Fig. 9 presents the shedding frequency based on FFT analysis of the time history of the lift (red line) and drag (blue line) coefficients obtained by the MDCM and DCM, respectively. The main shedding frequency obtained from the lift and drag coefficients show the same trend for both turbulence models. The Strouhal number, which characterizes the shedding frequency f, is defined as $St_c = fc/U_\infty = 0.175$ based on the ex-

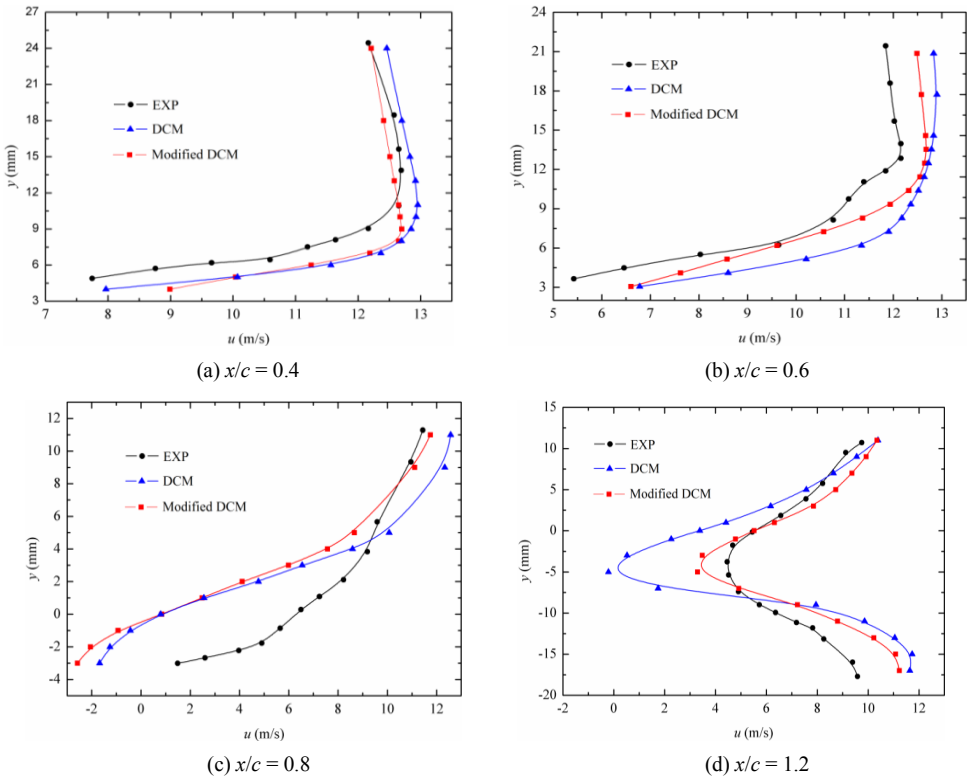

(a) x/c = 0.4 (b) x/c = 0.6

(c) x/c = 0.8 (d) x/c = 1.2

Fig. 10. Time-averaged streamwise velocity profiles at selected streamwise locations along the hydrofoil for cloud cavitation.

perimental measurements [25]. The predicted Strouhal number is calculated to be St_c = 0.197, which corresponds to the main cavity shedding frequency of 28.1 Hz for the MDCM. In the same manner, the Strouhal number is predicted to be St_c = 0.23 with the shedding frequency of f = 33 Hz for the DCM.

4.4 Characteristics of velocity distributions

Cavitation occurs when the local static pressure decreases and becomes less than the vapor pressure, which significantly varies the velocity distributions in the cavity regime. The time-averaged x-velocity was determined to analyze the distribution of velocity and its effect on the thickness of the cavity.

The time-averaged x-velocity component profiles along the wall-normal direction at four specified streamwise locations, that is, x/c = 0.4, 0.6, 0.8 and 1.2, are presented on the suction side of the hydrofoil, as shown in Fig. 10. These figures can be used to verify the capability and accuracy of these two different turbulence models for quantitatively predicting the cloud cavitation regime around a 2D hydrofoil. The thicker cavity in the streamwise direction, the larger velocity gradient in the wall-normal direction. Fig. 10 shows that the predicted velocity profiles obtained using the MDCM are more consistent with the experimental data than that of the DCM. Particularly, the MDCM predicts more accurate velocity values than the simulation results of the DCM at the position of x/c =1.2, which reveals that the MDCM is more capable than the original DCM in predicting the wake flow downstream at cloud cavitation.

4.5 Time-dependent visualization of cloud cavitation and reentrant jet flow

In this section, the details of cloud cavitation around the 2D Clark-Y hydrofoil at the cavitation number of σ = 0.8 are discussed to assess the performance of two different turbulence models. When the cavitation number decreases to 0.8, the sheet cavity moves toward the trailing edge, resulting in increasing unsteadiness and turbulence until transient cloud cavitation occurs. Comparisons of the predicted vapor fraction contours with the experimentally observed cavity structures from Ref. [26] within a typical flow cycle are shown in Fig. 11.

As observed in Fig. 11, the numerical predictions by both turbulence models are capable of capturing the initiation of the cloud cavity, its growth toward the trailing edge, and subsequent shedding, which are qualitatively consistent with the features observed experimentally. The same points between the predictions by both turbulence models are summarized in the subsequent paragraphs.

The predicted sheet cavity by both turbulence models almost show the same trend at the leading edge of the hydrofoil because the DCM is applied in both simulations. At $t = t_0$, the attached sheet cavity nearly disappears, whereas the cloud cavity generated from the collapse of the previous sheet cavity is still clearly visible near the trailing edge of the hydrofoil, as illustrated in Fig. 11(a). Subsequently, the quasi-steady sheet

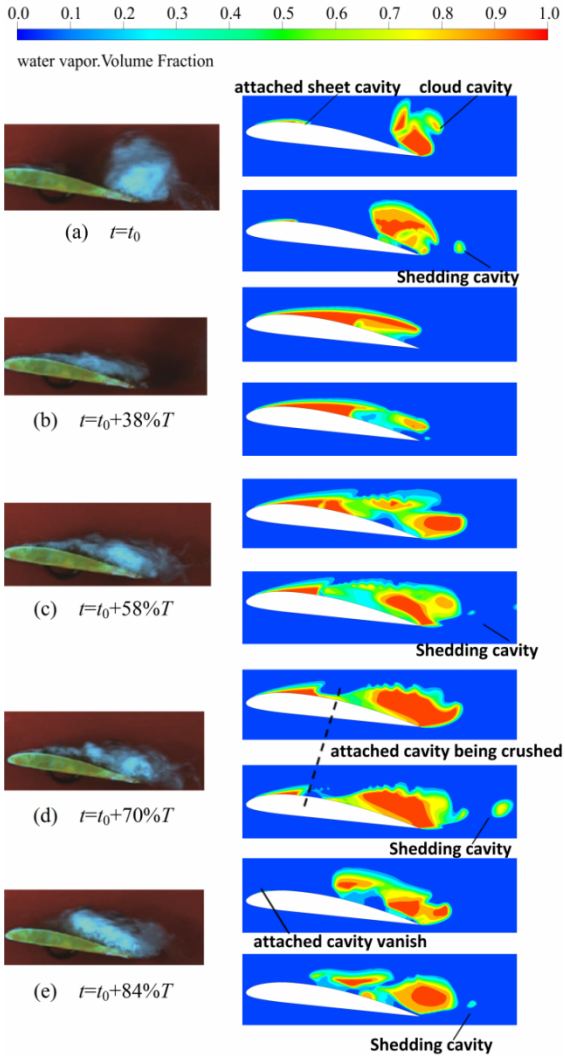

Fig. 11. Comparisons of cavity shape evolution between the simulation and the experiment. Left: experimental pictures from Ref. [26] are provided where available; right, top: Simulation results of the DCM; right, bottom: Simulation results of the MDCM.

cavity grows close to the trailing edge and to its maximum length at $t = t_0 + 38\ \%T$. Meanwhile, the cloud cavity near the trailing edge in the previous moment has shed downstream, as illustrated in Fig. 11(b).

As observed from the experimental results shown in Figs. 11(c) and (d), the sheet cavity near the leading edge gradually moves toward the trailing edge. This movement is induced by the reentrant jet, which forms and pushes the main flow toward the leading edge when the adverse pressure gradient is sufficiently strong to overcome the weaker momentum of the flow confined by the boundary layer; thus, the cavity structures are strongly affected by the development of the reentrant jet flow [27]. As the reentrant jet flow reaches the vicinity of the cavity near the leading edge, the sheet cavity is forced to shed downstream in the form of a cloud cavity. Then, a new cloud cavitation cycle starts, as shown in Fig. 11(e). The simulation results of both turbulence models can predict the

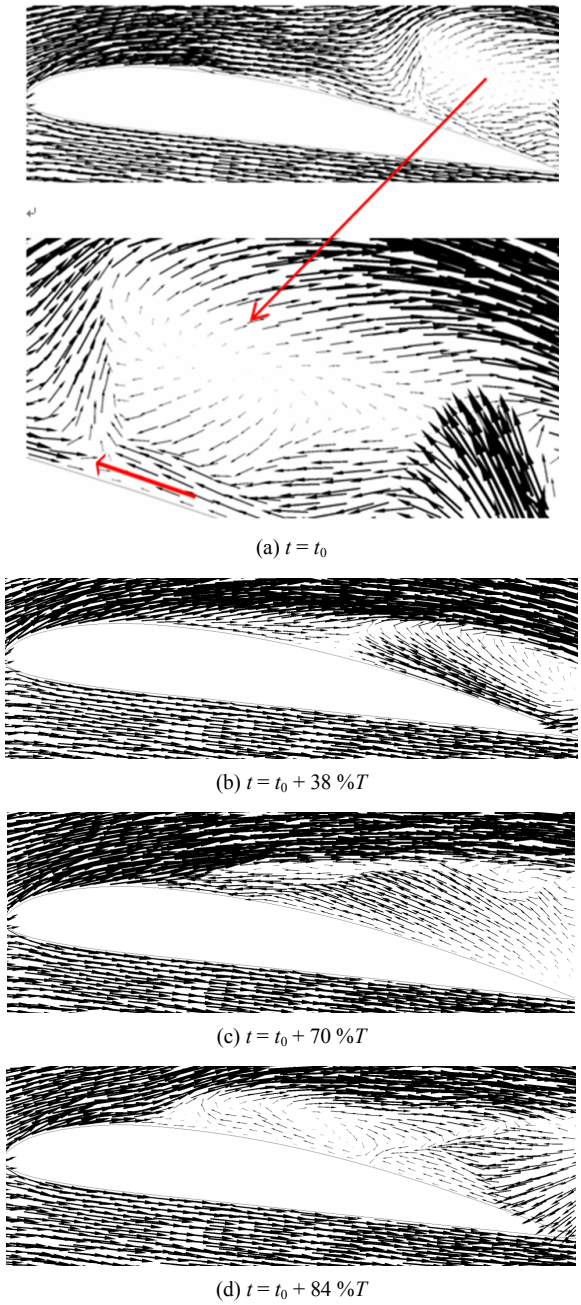

Fig. 12. Velocity distributions at four different time series for cloud cavitation using the MDCM.

movement of the attached cavity toward the trailing edge and the formation of a shedding cavity. However, as observed in Figs. 11(a), (c), (d) and (e), the MDCM predicts more shedding cavity than the DCM in the wake flow downstream, which corresponds to the fact that the MDCM not only works in the cavity closure near the suction surface of the hydrofoil but also the cavitating wake flow downstream.

The velocity distributions after being zoomed at the corresponding four different time series for cloud cavitation using the MDCM were captured to understand the relationship among cavity collapse, cavity shedding, and reentrant jet flow,

as shown in Fig. 12. As shown in Fig. 12(a), an initial reentrant jet flow is already generated near the trailing edge at $t = t_0$. Meanwhile, a vortex is also captured in the wake flow, which is in accordance with the formation of the cloud cavity shown in Fig. 11(a). The reentrant jet flow develops and moves toward the leading edge, and as a result, it almost covers half of the suction side of the hydrofoil, as shown in Fig. 12(b). Subsequently, the reentrant jet continually moves toward the leading edge and causes break-off of the detached sheet cavity, and the undetached cavity develops into a cloud cavity and moves toward the trailing edge, as shown in Figs. 12(c) and (d). In conclusion, the predicted vector distributions of cloud cavitation indicate that external flow governs the transport of shed vapor structures toward the trailing edge.

5. Conclusions

In the present study, a numerical simulation of flow around a 2D Clark-Y hydrofoil at a fixed attack angle of $\alpha = 8°$ with $Re = 6.14 \times 10^5$ for various cavitation numbers representing the non-cavitating and sheet/cloud cavitating flows is presented. Available experimental data in the literature are used to compare the simulation results of the unsteady and turbulent characteristics of cavitation dynamics and velocity field. The simulation is performed using the CFD solver ANSYS Fluent 14.5. The MDCM is proposed to close the turbulence model for cavitating flow by combining the strengths of the FBM and the original DCM. The most important findings are as follows:

(1) The MDCM is more capable and physical than the DCM in predicting the characteristics of the lift and drag forces of the hydrofoil under cavitating conditions.

(2) The MDCM is capable of predicting the unsteady and turbulent characteristics of cloud cavitation and can regulate the turbulent eddy viscosity in the cavitation and wake regions. By contrast, the DCM only acts in the cavitating region along the hydrofoil to limit the turbulent viscosity.

(3) The numerical results show self-oscillatory behavior at the cavitation number of $\sigma = 0.8$ because of the rapid changes of the length of cavity and the cloud cavity shedding downstream.

Acknowledgment

The authors gratefully acknowledge the financial support of the National Natural Science Foundation of China (No. 51206063), A Project Funded by the Priority Academic Program Development of Jiangsu Higher Education Institutions and the Jiangsu Government Scholarship for Overseas Studies and Scientific Research.

Nomenclature

ρ_m : Mass density of the mixture
μ_m : Molecular viscosity
μ_t : Turbulent viscosity
Re : Reynolds number
ρ_l : Density of liquid
ρ_v : Density of vapor
α_v : Volume fraction of vapor
μ_l : Liquid dynamic viscosity
μ_v : Vapor dynamic viscosity
S_e : Source terms for evaporation
S_c : Condensation processes
C_{dest} : Empirical constant, $C_{dest} = 2.0 \times 10^4$
C_{prod} : Empirical constant, $C_{prod} = 1.0 \times 10^3$
t_∞ : L_{ch}/U_∞
L_{ch} : Characteristic length
U_∞ : Free stream velocity
$k^{3/2}/\varepsilon$: Local turbulence length scale
λ : Filter size
C_μ : Empirical constant, $C_\mu = 0.09$
C_3 : Empirical constant, $C_3 = 1.0$
p_{out} : Pressure at the outlet that determines the cavitation numbers
p_{sat} : Saturation pressure of vapor
U_∞ : Free stream velocity
σ : Cavitation number

References

[1] C. E. Brennen, *Cavitation and bubble dynamics*, Cambridge University Press (2014).

[2] T. R. Chen, B. Huang, G. Y. Wang and K. Wang, Effects of fluid thermophysical properties on cavitating flows, *Journal of Mechanical Science and Technology*, 29 (10) (2015) 4239-4246.

[3] H. P. Wei, S. Fu, Q. Wu, B. Huang and G. Y. Wang, Experimental and numerical research on cavitating flows around axisymmetric bodies, *Journal of Mechanical Science and Technology*, 28 (11) (2014) 4527-4537.

[4] J. Y. Wu, G. Y. Wang and W. Shyy, Time-dependent turbulent cavitating flow computations with interfacial transport and filter-based models, *International Journal for Numerical Methods in Fluids*, 49 (7) (2005) 739-761.

[5] A. Kubota, H. Kato and H. Yamaguchi, A new modeling of cavitating flows: A numerical study of unsteady cavitation on a hydrofoil section, *Journal of fluid Mechanics*, 240 (1) (1992) 59-96.

[6] Y. Delannoy and J. L. Kueny, Cavity flow predictions based on the Euler equations, *ASME Cavitation and Multi-Phase Flow Forum,* 109 (1990) 153-158.

[7] O. Coutier‐Delgosha, J. L. Reboud and Y. Delannoy, Numerical simulation of the unsteady behaviour of cavitating flows, *International Journal for Numerical Methods in Fluids*, 42 (5) (2003) 527-548.

[8] A. Kubota, H. Kato and H. Yamaguchi, Unsteady structure measurement of cloud cavitation on a foil section using conditional sampling technique, *Journal of Fluids Engineering*, 111 (2) (1989) 204-210.

[9] A. K. Singhal, M. M. Athavale, H. Li and Y. Jiang, Mathematical basis and validation of the full cavitation model, *Journal of Fluids Engineering*, 124 (3) (2002) 617-624.
[10] C. L. Merkle, J. Z. Feng and P. E. O. Buelow, Computational modeling of the dynamics of sheet cavitation, *Proceedings of the 3rd International Symposium on Cavitation*, Grenoble, France (1998).
[11] R. F. Kunz, D. A. Boger, D. R. Stinebring, T. S. Chyczewski, J. W. Lindau, H. J. Gibeling, S. Venkateswaran and T. R. Govindan, A preconditioned Navier-Stokes method for two-phase flows with application to cavitation prediction, *Computers & Fluids*, 29 (8) (2000) 849-875.
[12] I. Senocak and W. Shyy, A pressure-based method for turbulent cavitating flow computations, *Journal of Computational Physics,* 176 (2) (2002) 363-383.
[13] J. L. Reboud, B. Stutz and O. Coutier-Delgosha, Two phase flow structure of cavitation: Experiment and modeling of unsteady effects, *Proceedings of the Third Symposium on Cavitation,* Grenoble, France (1998).
[14] O. Coutier-Delgosha, R. Fortes-Patella and J. L. Reboud, Evaluation of the turbulence model influence on the numerical simulations of unsteady cavitation, *Journal of Fluids Engineering*, 125 (1) (2001) 38-45.
[15] P. R. Spalart, Strategies for turbulence modelling and simulations, *International Journal of Heat and Fluid Flow*, 21 (3) (2000) 252-263.
[16] J. Wu, W. Shyy and S. T. Johansen, Filter-based unsteady RANS computations for single-phase and cavitating flows, *ASME 2004 Heat Transfer/Fluids Engineering Summer Conference, American Society of Mechanical Engineers*, 3 (2004) 469-477.
[17] S. S. Girimaji, Partially-averaged Navier-Stokes model for turbulence: A Reynolds-averaged Navier-Stokes to direct numerical simulation bridging method, *Journal of Applied Mechanics*, 73 (3) (2006) 413-421.
[18] B. Huang, Y. L. Ying, G. Wang and W. Shyy, Combined experimental and computational investigation of unsteady structure of sheet/cloud cavitation, *Journal of Fluids Engineering,* 135 (7) (2013) 071301.
[19] J. Kim and J. Lee, Numerical study of cloud cavitation effects on hydrophobic hydrofoils, *International Journal of Heat and Mass Transfer*, 83 (2015) 591-603.
[20] J. H. Seo and S. K. Lele, Numerical investigation of cloud cavitation and cavitation noise on a hydrofoil section, *Proceedings of the 7th International Symposium on Cavitation CAV*, August, Ann Arbor, Michigan, USA.
[21] A. Ducoin, B. Huang and L. Y. Yin, Numerical modeling of unsteady cavitating flows a round a stationary hydrofoil, *International Journal of Rotating Machinery* (2012) 215678.
[22] S. T. Johansen, J. Y. Wu and W. Shyy, Filter-based unsteady RANS computations, *International Journal of Heat and Fluid Flow*, 25 (1) (2004) 10-21.
[23] ANSYS FLUENT, *ANSYS Fluent 14.5 Documentation*.
[24] N. Ochiai, Y. Iga, M. Nohmi and T. Ikohagi, Numerical prediction of cavitation erosion intensity in cavitating flows around a Clark Y 11.7% hydrofoil, *Journal of Fluid Science and Technology*, 5 (3) (2010) 416-431.
[25] G. Wang, I. Senocak, W. Shyy, T. Ikohagi and S. L. Cao, Dynamics of attached turbulent cavitating flows, *Progress in Aerospace Sciences*, 37 (6) (2001) 551-581.
[26] C. L. Hu, G. Y. Wang, G. H. Chen and B. Huang, A modified PANS model for computations of unsteady turbulence cavitating flows, *Science China Physics Mechanics and Astronomy*, 57 (10) (2014) 1967-1976.
[27] B. Huang, G. Y. Wang, Z. Y. Yu and S. G. Shi, Detached-eddy simulation for time-dependent turbulent cavitating flows, *Chinese Journal of Mechanical Engineering*, 25 (3) (2012) 484-490.

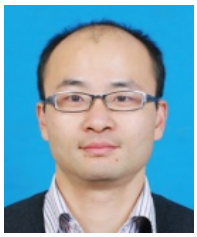

Zhong Li was born in 1979 in China. He is currently an Associate Professor at the School of Energy and Power Engineering of Jiangsu University. His main research interests are multiphase flow within pumps and optimal design of fluid machineries.